Explosion-Generated Infrasound Recorded on Ground and Airborne Microbarometers at Regional Distances

by E. F. Young, D. C. Bowman, J. M. Lees, V. Klein, S. J. Arrowsmith, and C. Ballard

ABSTRACT

Recent work in deploying infrasound (low-frequency sound) sensors on aerostats and free-flying balloons has shown them to be viable alternatives to ground stations. However, no study to date has compared the performance of surface and free-floating infrasound microbarometers with respect to acoustic events at regional (100s of kilometers) range. The prospect of enhanced detection of aerial explosions at similar ranges, such as those from bolides, has not been investigated either. We examined infrasound signals from three 1-ton trinitrotoluene (TNT) equivalent chemical explosions using microbarometers on two separate balloons at 280- to 400-km ranges and ground stations at 6.3- to 350-km ranges. Signal celerities were consistent with acoustic waves traveling in the stratospheric duct. However, significant differences were noted between the observed arrival patterns and those predicted by an acoustic propagation model. Very low-background noise levels on the balloons were consistent with previous studies that suggest wind interference is minimal on freely drifting sensors. Simulated propagation patterns and observed noise levels also confirm that balloon-borne microbarometers should be very effective at detecting explosions in the middle and upper atmosphere as well as those on the surface.

INTRODUCTION

Infrasound is defined as acoustic waves below the threshold of human hearing, generally 20 Hz or lower. Infrasound waves propagate over long distances with little absorption compared with higher frequency waves—classical attenuation is proportional to $1/f^2$ (Evans *et al.*, 1972), in which f is the wave's frequency. These signals often serve as remote tracers of ground-based or atmospheric disturbances. Surface sources include earthquakes (Arrowsmith *et al.*, 2012), tsunamis (Le Pichon *et al.*, 2005), and volcanic eruptions (Matoza *et al.*, 2017), as well as chemical and nuclear explosions (Green and Bowers, 2010); atmospheric sources include bolides (ReVelle, 1976), rocket launches (Blom *et al.*, 2016), and spacecraft re-entry (Ishihara *et al.*, 2012). The International Monitoring

System Division of the Comprehensive Test Ban Treaty Organization (IMS/CTBTO) has 49 infrasound stations at present (with a total of 60 planned) to listen for treaty violations.

Because infrasound refraction is a function of wind and temperature fields, the Atmospheric dynamics Research Infra-Structure in Europe (ARISE) project uses the IMS infrasound stations (and additional instrumentation) to reconstruct 3D images of the troposphere, stratosphere, and mesosphere to improve short- and medium-range weather forecasting (Blanc *et al.*, 2017). However, Earth surface infrasound sensors often suffer from wind noise, which limits their sensitivity depending on weather conditions. Sensors also cannot be deployed on the ocean, constraining the geographic distribution of ground infrasound stations.

The potential advantages of balloon-borne infrasound sensors were realized over a half-century ago (Wescott, 1964; Weaver and McAndrew, 1995). Recent experiments have suggested that whereas free-floating balloons have little to no background wind noise (Bowman and Lees, 2017), wind noise is often a major limiting factor for ground-based sensors. Balloons are not limited to land but can travel over the ocean as well. Regions of the atmosphere centered around temperature minima can serve as infrasound wave guides (e.g., Waxler, Evers, *et al.*, 2015) that they may be able to capture.

Under ideal conditions, ground infrasound sensors can detect aerial explosions as small as 1.8 kg at altitudes up to 95 km (Stroud *et al.*, 1960). Balloon-borne microbarometers should be even more sensitive to these events because they are closer to the source and suffer very little wind noise. This makes them ideal platforms for capturing infrasound from bolides. These signals contain information on the size and speed of the object and therefore shed light on different populations of small Earth impactors (ReVelle, 1976; Silber and Brown, 2014).

Recently, Bowman and Lees (2017) showed that ocean-generated infrasound was observable on balloons in the stratosphere even when nearby ground stations did not record it. In 2017, the Heliotrope experiment captured ground explosion signals on multiple balloon platforms at a range of 150 km

(Bowman and Albert, 2018). Microbarometers on tethered balloons have been used to characterize infrasound from volcanic eruptions (Jolly et al., 2017), buried chemical explosions (Bowman et al., 2014), and ground motion from a seismic hammer (Krishnamoorthy et al., 2018). Several decades ago, Banister and Hereford (1991) used pressure and acceleration sensors on dropsondes to capture powerful infrasound signals from buried and surface explosions.

However, to our knowledge, no experiment has investigated infrasound from ground explosions recorded on surface and airborne sensors at multiple altitudes and ranges of several hundred kilometers or the ability of high-altitude stations to detect aerial explosions.

We report results from three 1-ton trinitrotoluene (TNT) equivalent explosions recorded on a ground and balloon-borne microbarometer network in eastern New Mexico on 28 September 2016. Observed signals are described and compared with waveform and amplitude predictions for stratospherically ducted infrasound. The spatial and temporal pattern of observed arrivals is related to modeled propagation patterns. The modeling is then extended to consider aerial explosions such as those from bolides.

METHODS

In this experiment, we arranged for Energetic Materials Research and Testing Center (EMRTC) to set off three large explosions (3000 lb ammonium nitrate/fuel oil, equivalent to about 1 ton of TNT) from a site outside of Socorro, New Mexico, on 28 September 2016 at noon, 2 p.m., and 4:30 p.m. (local time; 18:00, 20:00, and 22:30 UTC). The exact location of the epicenter was 34.07057° N latitude, 106.9797° W longitude (Table 1). Times for shots 1 and 2 are accurate to within 1 s, but shot 3 may have a timing error of approximately 1 s. These explosions were coordinated with a National Aeronautics and Space Administration (NASA) balloon flight that was launched from Ft Sumner, New Mexico, about 250 km east of Socorro. The NASA balloon lifted off at 14:21 UTC and reached its float altitude of 37 km at approximately 17:00 UTC (Table 1). NASA's primary payload on the balloon flight was the Wallops Arc-Second Pointing system (WASP), but two separate infrasound sensing packages were also on board: Stratospheric Infrasound Sensitivity Experiment (SISE, from Southwest Research Institute) and UNC-Sandia Infrasound Experiment (USIE, from UNC Chapel Hill and Sandia National Laboratories). We also built and launched a small solar balloon to listen for infrasound signals at a lower altitude. This solar balloon was constructed of clear plastic darkened with charcoal powder; it was a prototype of the Heliotrope flight system described in Bowman and Albert (2018). The solar balloon was launched at 15:57 UTC and reached its float altitude at approximately 18:45 UTC (Table 1). The

| Event	Latitude (°)	Longitude (°)	Time (UTC) (yyyy/mm/dd hh:mm:ss)
SISE/USIE launch	34.489	−104.218	2016/09/28 14:21:05
Solar balloon launch	34.448	−104.161	2016/09/28 15:57:00
SISE/USIE float	34.740	−103.832	2016/09/28 16:57:00
Shot 1	34.072	−106.984	2016/09/28 18:00:00
Solar balloon float	34.682*	−103.620*	2016/09/28 18:46:00
Shot 2	34.072	−106.984	2016/09/28 20:00:00
Shot 3	34.072	−106.984	2016/09/28 22:29:59 ±1 s
SISE/USIE termination	34.376	−102.366	2016/09/28 23:46:28
SISE/USIE impact	34.400	−102.194	2016/09/29 00:25:15
Solar balloon termination	35.478*	−104.519*	2016/09/29 01:00:00*
Solar balloon impact	35.632	−103.890	2016/09/29 02:47:17

Table 1
Locations and Timeline

SISE, Stratospheric Infrasound Sensitivity Experiment; USIE, UNC-Sandia Infrasound Experiment.
*Estimated value.

solar balloon carried a Gem infrasound sensor/logger package (Anderson et al., 2018). The USIE payload carried InfraBSU infrasound sensors and a Chaparral 60 infrasound sensor, logging signals at 200 Hz to Omnirecs Datacube loggers. The InfraBSU microbarometers are differential pressure transducers with two ports, one of which is capped with a flow filter (a short capillary tube) to allow gradual equilibration with the ambient air pressure (Marcillo et al., 2012). The Chaparral 60 is a compact low-power infrasound microbarometer with similar frequency response characteristics as those of InfraBSU (Slad and Merchant, 2016). The SISE payload carried five differential pressure transducers (similar to the InfraBSUs) and five reference transducers. The reference transducers had flow filters on both ports: they were intended to serve as accelerometers to characterize and remove signals caused by the payload motion (e.g., pendulum swinging) that could otherwise be confused with infrasound waves.

Sensors used in the airborne experiment had flat frequency responses above about 20 s on the Earth's surface, but the low-frequency corner decreases to several hundred seconds at high altitudes because of increasing acoustic capacitance at lower ambient pressure (Mentink and Evers, 2011).

Figure 1 shows the geographic locations of the five infrasound ground stations and the trajectories of the two balloons, and Table 1 describes the location and times of events during the experiment. Both balloons were launched about 250 km east of Socorro and traveled to the east during ascent. The solar balloon drifted to the northwest when it reached float altitude, but we had to estimate part of its trajectory because we did not have continuous Global Positioning System (GPS) positions when the balloon was above 13 km. The NASA balloon also traveled to the east, with a small jog to the northwest during ascent.

The closest ground station (labeled PASS in Fig. 1) consisted of a single Hyperion microbarometer with a porous
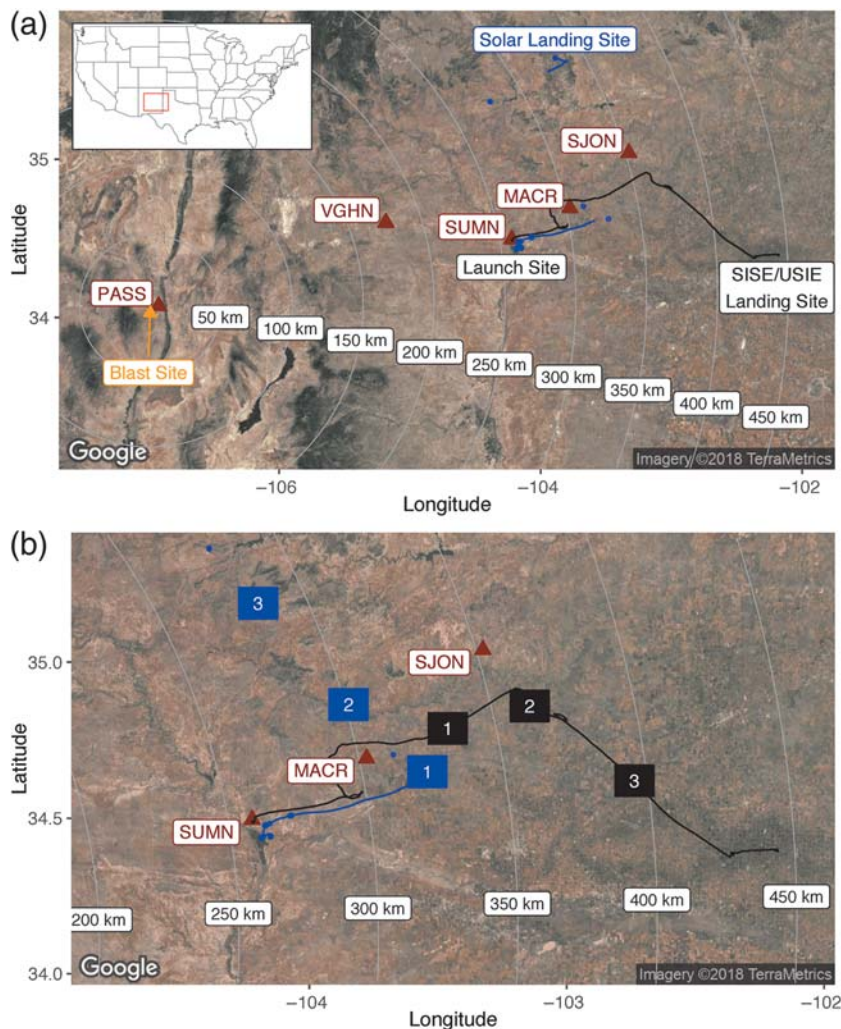
▲ **Figure 1.** (a) Epicenter near Socorro, New Mexico, the five ground stations (PASS, VGHN, SUMN, MACR, and SJON) and the National Aeronautics and Space Administration (NASA) and solar balloon trajectories (lines originating from Ft Sumner in black and blue, respectively). The PASS ground station is only 5.6 km from the epicenter, but the SUMN ground station is adjacent to the Ft Sumner airport from where the balloons were launched. (b) Close-up of the balloon trajectories with the balloon positions marked at the times of the first, second, and third explosions. The solar balloon positions are interpolations because the payload did not record continuous Global Positioning System (GPS) positions above 13 km.

soaker hose wind noise mitigation system. The other stations used two Hyperion microbarometers, separated by about 2 m, each with high-frequency wind shrouds. The ground stations were all digitized on RefTek 130 loggers and had flat frequency responses across the band of interest. The five ground stations were deployed to the east of EMRTC at distances ranging from 5.6 to 350 km (Fig. 1). They were deployed to the east of Socorro because the direction of winds at the NASA balloon float altitudes was west to east.

Infrasound signals from the explosions were identified by searching for impulsive waveforms arriving at each station in a time window consistent with celerities between 220 and 350 m/s. Celerity is the distance divided by travel time for

the purposes of this article. Because the 1-ton TNT equivalent explosions used in this experiment should have a peak frequency of 1–2 Hz (Gi and Brown, 2017), the data were bandpassed in the 0.5- to 8-Hz band.

Visual inspection revealed candidates for all three explosions at station PASS, shots 2 and 3 at VGHN, shot 2 on the solar balloon, shots 1 and 2 on the NASA helium balloon, and shot 1 at SUMN. Where multiple sensor channels were available (NASA helium balloon, ground stations VHGN, SUMN, MACR, and SJON), we crosscorrelated the collocated waveforms to search for additional signals. This revealed shot 2 on MACR and shot 3 on the NASA helium balloon. The observed acoustic celerities fall within expected tropospheric and stratospheric ranges for each observation (see Table 2).

Acoustic transmission loss modeling was performed via the range-independent wide-angle Padé parabolic equation method as implemented in the open-source *ncpaprop* software package (Waxler, Hetzer, and Velea, 2015). This algorithm computes transmission loss across a 2D slice of atmosphere over rigid ground via the effective sound speed approximation using intrinsic attenuation values from Sutherland and Bass (2004). We used a 3-Hz wave originating at EMRTC and traveling along the azimuth defined by the source and the NASA balloon (75.2°, 74.9°, and 79.9° from the north for each explosion, respectively). This was the approximate peak frequency observed on infrasound arrivals in the data (slightly higher than predicted). We derived effective sound speed using temperature and wind velocity profiles over EMRTC from the Ground to Space model (Drob *et al.*, 2003). We compared the Ground to Space wind profiles with the horizontal motion of the zero pressure balloon during ascent and float using the difference in the average position of on board GPS units over successive 100-s windows.

RESULTS

Figure 2 shows pressure data recorded on the NASA balloon, the solar balloon, and ground station VGHN during the explosion series. Both the solar balloon and the NASA balloon exhibit long-period pressure oscillations due to "cork bobbing" around their neutral buoyancy altitude (Anderson and Taback, 1991). The solar balloon reached neutral buoyancy at approximately 18:45 UTC. Prior to this, wind rushing past the microbarometer outlet during the ascent dominated the pressure time series. This is particularly evident in the 2-s to 5-Hz band (Fig. 2b). When they were at neutral buoyancy, however, the

Table 2
Infrasound Detections

Shot	Station	Range (km)	Azimuth (°)	Elevation (km)	Amplitude (Pa)*	Celerity (m/s)
1	PASS	5.81	88.4	1.65	28	352 ± 0.3
	SUMN?	259	78.7	1.26	0.53	297 ± 0.7
	USIE	333	75.2	37.2	0.062	293 ± 0.4
2	PASS	5.81	88.4	1.65	16	350 ± 0.5
	VGHN	176	69.9	1.80	4.1	281 ± 0.3
	SOLR	301 ± 10	72.1 ± 2	16.0 ± 0.5	0.10	300 ± 10[†]
	MACR?	303	75.9	1.44	0.11	299 ± 0.5
	USIE	363	74.9	37.0	0.020	293 ± 0.07
3[‡]	PASS	5.81	88.4	1.65	20	349 ± 19
	VGHN	176	69.9	1.80	1.8	281 ± 0.4
	USIE	395	79.9	35.8	0.017	296 ± 0.2

The ? means a tentative detection of acoustic signal from the ground.
*Measured peak-to-peak in the 0.5–5 Hz band.
[†]The solar balloon's position is uncertain because of lack of continuous Global Positioning System (GPS) above 13-km altitude.
[‡]Shot 3 timing has a ±1 s uncertainty, resulting in poor celerity resolution for nearby stations.

balloons had much lower background noise levels than the ground station in this band.

Sensors on the NASA balloon captured all three explosions (Fig. 3). However, the SISE sensors experienced significant electronic interference and therefore poorer signal-to-noise ratios (SNRs) than the USIE sensors; they are not discussed further. The first explosion produced three arrivals on the NASA balloon (see Fig. 4): the second and third arrivals are M-shaped waves that have flipped polarity with respect to each other. The second and third explosions produced only one arrival on the NASA balloon. The single sensor on the solar balloon observed the second explosion (Fig. 3 and Table 2). All three explosions were observed on the PASS ground station (5.6 km from the epicenter), and the second two explosions were observed by the VGHN ground station at a range of 180 km. Two signals with low SNR were identified on the three ground stations located beyond 180 km.

Ground Station Detections
Only two of the five ground stations (PASS and VGHN, at ranges of 5.81 and 176 km; see Fig. 1) captured clear signals from any of the three explosions. Two others (SUMN and MACR, at ranges of 259 and 303 km) had possible observations of shots 1 and 2, respectively, although the signals had poor SNRs. The farthest station (SJON) was only active for the latter two explosions, but neither of them was observed. The celerity to the PASS station (just 5.6 km from the epicenter) was close to 350 m/s for all three explosions, but the celerity to the VGHN station in shots 2 and 3 was 281 m/s in both cases.

Solar and NASA Balloon Detections
The sensor on the solar balloon only captured the second explosion. Wind noise during its ascent may have obscured the signal from the first explosion (Fig. 2). The trajectories of both balloons were toward the east during ascent, but the solar balloon then drifted in a northwest direction when it reached its float altitude near 16 km. It is not obvious why the solar balloon did not observe the third explosion. The solar balloon was actually closer to the epicenter at the time of the third explosion than it was during the second one, yet the second explosion is clearly observed, and the third one is not.

Table 2 and Figure 3 outline infrasound observations from the three explosions. The solar balloon observed a second-explosion infrasound amplitude of about 0.095 Pa, when the balloon was about 300 km from the explosion. In contrast, the NASA balloon observed a first-explosion amplitude of about 0.066 Pa, a second-explosion amplitude of 0.020 Pa, and a third-explosion amplitude of 0.017 Pa, at positions that were 333, 363, and 395 km east of the epicenter, respectively. The amplitude of the pressure wave is expected to scale with ambient conditions as follows:

$$p_1 = p_0 \sqrt{\frac{c_1 \rho_1}{c_0 \rho_0}}, \tag{1}$$

in which c is the speed of sound, ρ is the density, and p is the amplitude of the pressure wave (Rayleigh, 1894; Lighthill, 1978). In other words, as an acoustic wave propagates to different regions, the amplitude of the wave scales with the square root of the specific acoustic impedance. An empirical study by Whitaker and Mutschlecner (2008) using data from nuclear and chemical explosions at about 200-km range found that stratospherically ducted infrasound suffers attenuation via

$$p = p_r 10^{-kV_d} \left(\frac{R_r}{R}\right)^S, \tag{2}$$

in which p is the amplitude at the receiver, p_r is amplitude at a reference distance, V_d is the wind speed from source to receiver at 45- to 55-km altitude, S is an empirical constant with value 1.45, and k is an empirical constant with a value of 0.018. According to equations (1) and (2), the amplitude ratio at two receivers that capture a stratospheric infrasound arrival is

$$\frac{p_1}{p_0} = \sqrt{\frac{c_1 \rho_1}{c_0 \rho_0}} \left(\frac{R_0}{R_1}\right)^S, \tag{3}$$

in which R_1 and R_0 are source–receiver distances. The expression assumes the receivers lie along the same azimuth with respect to the source. In equations (2) and (3), S represents an empirically
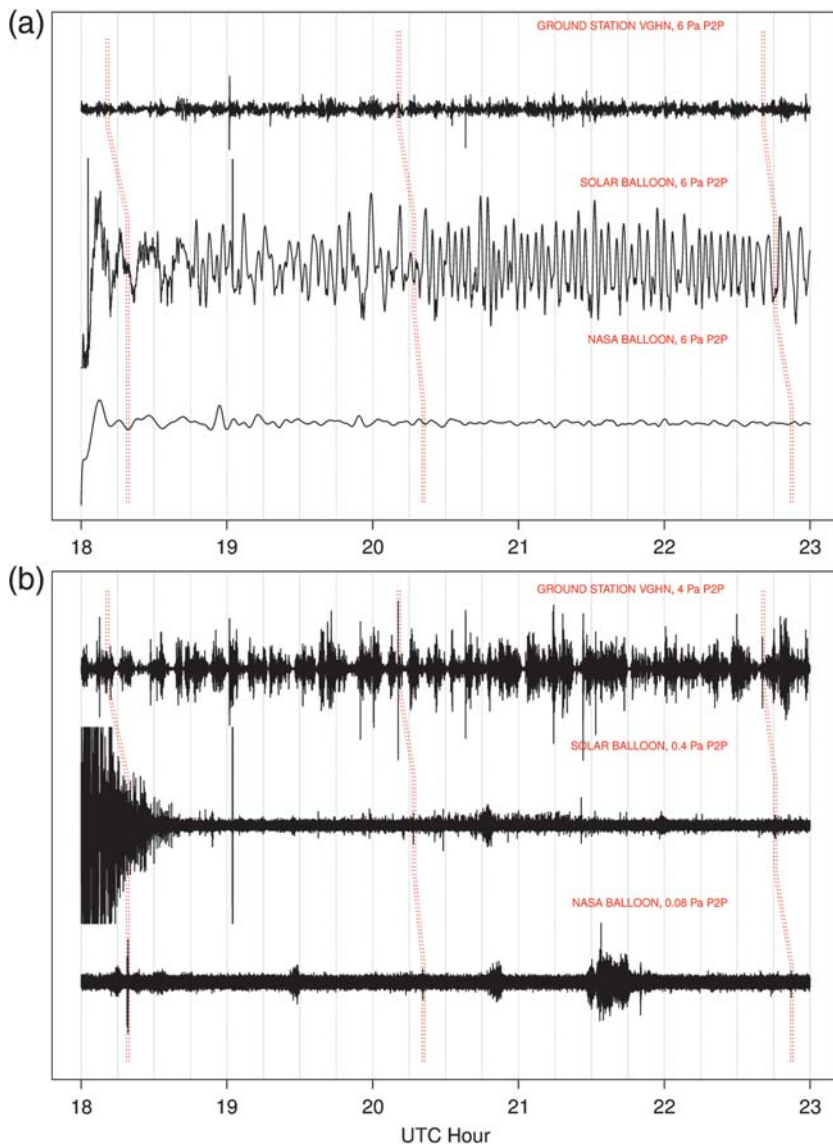
▲ **Figure 2.** Pressure time series recorded on ground station VGHN, the solar balloon, and the NASA/Helium balloon filtered in (a) the 1000-s to 25-Hz band and (b) the 2-s to 5-Hz band. Dotted red lines outline the time windows for observed and expected explosion infrasound arrivals shown in Figure 3. Interference from the satellite tracker caused spikes in the solar balloon record just after 18:00 and 19:00 UTC. A Butterworth band-pass filter was used.

derived attenuation factor for the stratospheric duct. Its value suggests that the stratospherically refracted infrasound loses amplitude more rapidly than spherically expanding waves in non-dissipative isotropic media.

For the second explosion, the measured pressure amplitude at the solar balloon is about one-fortieth of the pressure amplitude at the VGHN ground station, and the amplitude on the NASA balloon was one-fifth of that measured on the solar balloon. According to equation (3), the expected solar/VGHN amplitude ratio is 0.18 ± 0.05, and the NASA/solar amplitude ratio is 0.15 ± 0.1. Here, we assume each receiver pair lies along the same azimuth (in reality, they deviate by $< 5°$), and

we use atmospheric data from the 20z Ground to Space model output. The NASA/solar observed ratio of 0.20 is close to the predicted value of 0.15, but the observed solar–VGHN ratio of 0.024 is much less than the predicted ratio of 0.18. Amplitude ratios via the transmission loss estimates from *ncpaprop* shown in Figure 5 are 0.33 for the NASA–solar pair and 38000 for the solar–VGHN pair after scaling for specific acoustic impedance. The NASA–solar ratio is close to the observed value in this case as well, but the solar–VGHN ratio is orders of magnitude too high because the ground station is predicted to be in the shadow zone.

DISCUSSION

Observations versus Predictions
One of the primary goals of detonating explosions was to compare the sensitivity of ground-based and balloon-borne sensors. That goal was complicated by refractive effects that dominate the signals received by the five ground stations and both balloons. Three of the stations (SUMN, MACR, and SJON) did not record high-SNR arrivals for any of the explosions, and the other two stations (PASS and VGHN) recorded large variability in signal amplitude from explosion to explosion even though all three explosions used the same configurations of explosive material.

The transmission loss predictions for the ground-based stations do not match the observations: whereas the VGHN, MACR, and SJON stations are in shadow zones for all three explosions, station SUMN is expected to receive a strong signal in all three cases (Fig. 5). In fact, whereas the SUMN station reported only one low amplitude signal, the VGHN station showed no record of shot 1 but strong signals from shots 2 and 3 (with peak-to-peak amplitudes of 4 and 1.8 Pa, respectively). Predicted amplitude ratios calculated via Whitaker and Mutschlecner (2008) and *ncpaprop* agreed with the solar balloon versus NASA balloon observations but not for the solar balloon versus ground station VGHN. The positive performance of the Whitaker and Mutschlecner (2008) model is not surprising because the SISE/USIE experiment used relatively low yield explosions at similar ranges; extrapolating the model beyond these constraints should be done with caution (e.g., Le Pichon *et al.*, 2009). The second explosion may have had some refractive focusing at the VGHN station—after all, the third explosion had an amplitude of 1.8 Pa, about 40% of the second explosion amplitude, and the first explosion was not observed at VGHN at all. The NASA balloon recorded a first-explosion amplitude that
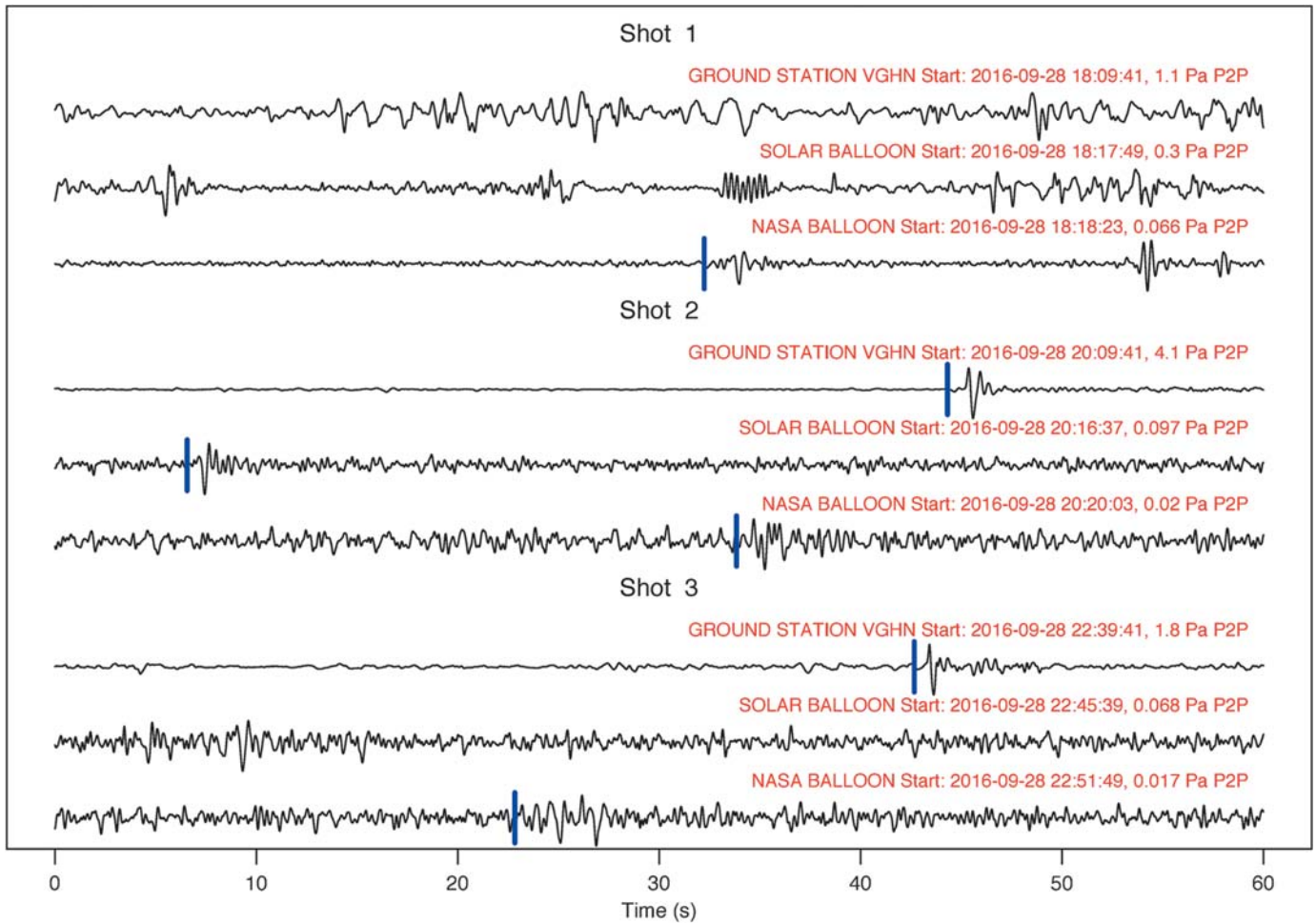
▲ **Figure 3.** Signals from three sites (ground station VGHN, the solar balloon, and the NASA/Helium balloon) are shown for each of the three Energetic Materials Research and Testing Center (EMRTC) explosions (shots 1, 2, and 3). Time series are aligned by a celerity of 302 m/s with respect to the source. A Butterworth filter with a 0.5- to 5-Hz passband has been applied to each signal. First arrival picks are shown in blue. On shot 1, the NASA balloon shows second and third arrivals, 18 and 23 s after the initial observation.

was six times higher than the second- or third-explosion amplitudes despite an increase in range of only 10% or 20%. The celerities (Table 2) are typical of infrasound waves that are refracted from the stratosphere (Negraru *et al.*, 2010). We interpret these amplitude variations as resulting from the focusing and defocusing effects of the acoustic velocity structure of the atmosphere.

The ground stations (five sites spread over 350 km) and two balloon payloads represent a sparse network (see Fig. 1), but they still potentially constrain the wind and temperature fields at the explosion times. Infrasound arrival patterns on SUMN and VGHN suggest that the downward-directed rays near the 220-km mark were shifted toward the epicenter relative to the model predictions in Figure 5. Two mechanisms could account for that shift: stronger westerly winds in real life than in the G2S model (although balloon drift rates were within 5–10 km/hr of the G2S values; see Fig. 6) or a steeper turn at the peak of the ray bundle caused by a larger vertical temperature gradient near 40-km altitude. Alternatively, the observations at the VGHN station where none were predicted

could be the result of fine scale atmospheric fluctuations such as gravity waves. These waves are below the resolution of the G2S model but can have dramatic effects on infrasound propagation (Green *et al.*, 2011). Indeed, oscillations in the zonal velocity of the NASA balloon between 20- and 30-km altitude (Fig. 6) are similar to gravity wave wind perturbations at similar elevations reported in Chunchuzov *et al.* (2015) and Bowman and Albert (2018).

Shot 1 produced multiple arrivals on the NASA balloon. The polarity change of the second two arrivals is consistent with passage through caustics in the stratospheric acoustic duct (Waxler *et al.*, 2008). Similar waveforms have been reported on other airborne and ground-based experiments (Lonzaga *et al.*, 2015; Bowman and Albert, 2018). These arrivals constrain temperature and wind gradients because they are functions of sound speed over the specific trajectories taken by the separate ray bundles. We suggest that they could be used to characterize local variability at the ray turning points in the middle-upper stratosphere.
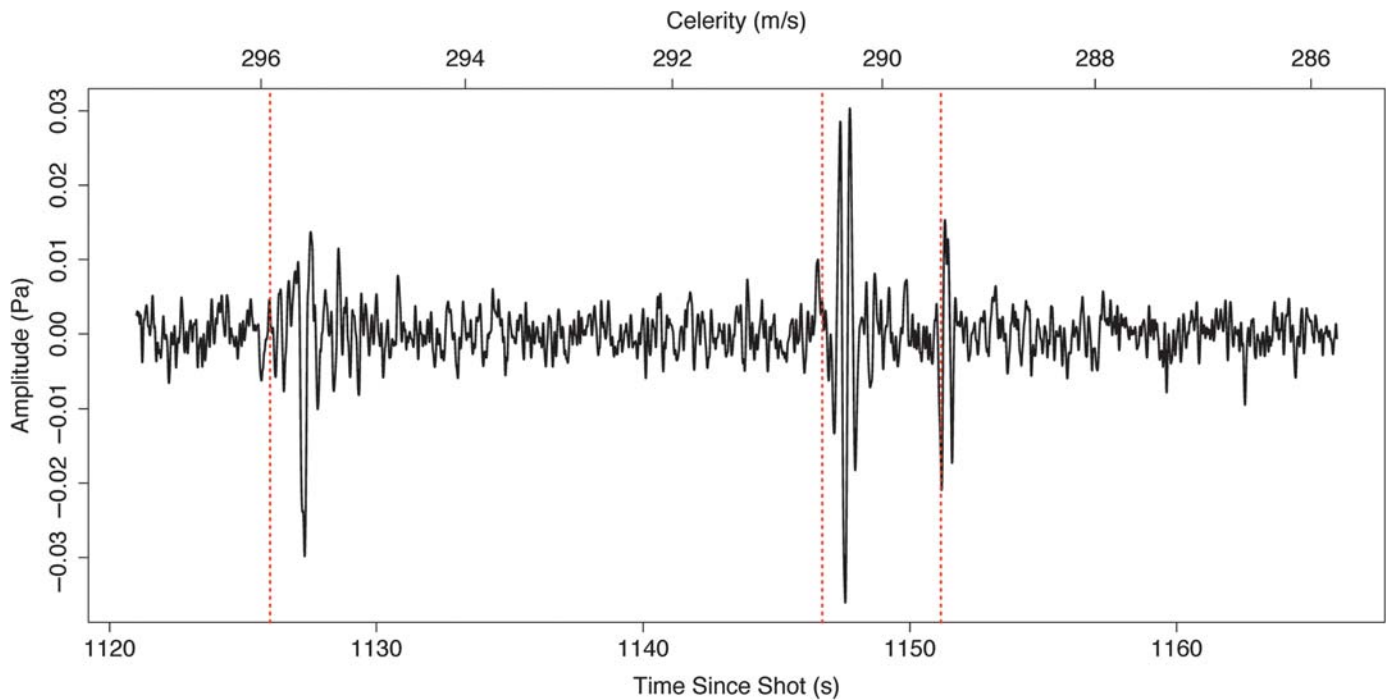
▲ **Figure 4.** Close-up of the three arrivals following shot 1 as seen by microbarometers on the NASA balloon. A 5 s to 10 Hz Butterworth filter was applied.

Ground versus Stratosphere

One putative advantage of balloon-borne sensors is that there should be virtually no wind noise on the free-floating platforms.

Results from the flights described in Bowman and Lees (2017) are in general agreement with this assertion, but high levels of electronic noise in the data made the actual pressure background difficult to determine. Design changes incorporated in the USIE payload reduced these noise sources, allowing a more direct comparison with ground sensors. Figure 7 shows pressure spectra recorded on USIE and the solar balloon versus local ground stations and the IMS infrasound noise model presented in Brown *et al.* (2014). The balloon-borne stations have much lower noise levels than ground station PASS (with a soaker hose wind noise reduction system) and station VGHN (with a high-frequency wind shroud). Airborne stations show a clear microbarom peak, but ground stations do not; this is in agreement with results presented in Bowman and Lees (2017). Finally, the balloon sensors fall within the background noise range of the IMS stations even after acoustic impedance contrasts are accounted for. This indicates that noise levels during SISE/USIE were slightly lower than those recorded in the lower stratosphere during the Heliotrope experiment (Bowman and Albert, 2018). A single balloon-borne sensor in the stratosphere has similar noise levels as a typical IMS station and a lower background than a single sensor on the ground with an elementary wind reduction system (e.g., soaker hoses and shrouds).

Does this mean that balloon-borne sensors are universally preferable to ground-based stations? Not necessarily—recall that the wave amplitude decreases with altitude, roughly scaling with the square root of density (equation 1). The altitude that yields the best sensitivity depends on noise sources besides wind noise, such as that produced by amplification and digitization electronics.

Ground-based stations are often configured with sensors separated by baselines of several hundred meters to help identify the propagation direction. Array-based signal detection schemes leverage this configuration to extract faint signals that would be very difficult to capture using single sensors as described here or via the sparse airborne network presented in Bowman and Albert (2018). Indeed, the required horizontal separation distances would be difficult to achieve on a single balloon payload. Ground-based stations are persistent and generally require little maintenance. Balloons do not maintain position, although some station keeping is possible if a balloon can change altitude. Balloon flight durations are probably limited to a few hundred days—the 1960s Global HOrizontal Sounding Technique (GHOST) program's longest balloon flight was 744 days (Lally, 1967). On the other hand, an advantage of balloon payloads is that they can be deployed over oceans or mountainous terrain.

Prospects for Bolide Detection

There are science cases for which a balloon in the stratosphere is particularly effective. For example, a balloon-borne sensor is well suited to detect bolides that deposit energy within the stratospheric duct. We modeled hypothetical explosions at 30-km altitude (Fig. 5a,c,e) in addition to the ground explosions that actually occurred at EMRTC (Fig. 5b,d,f). Infrasound is
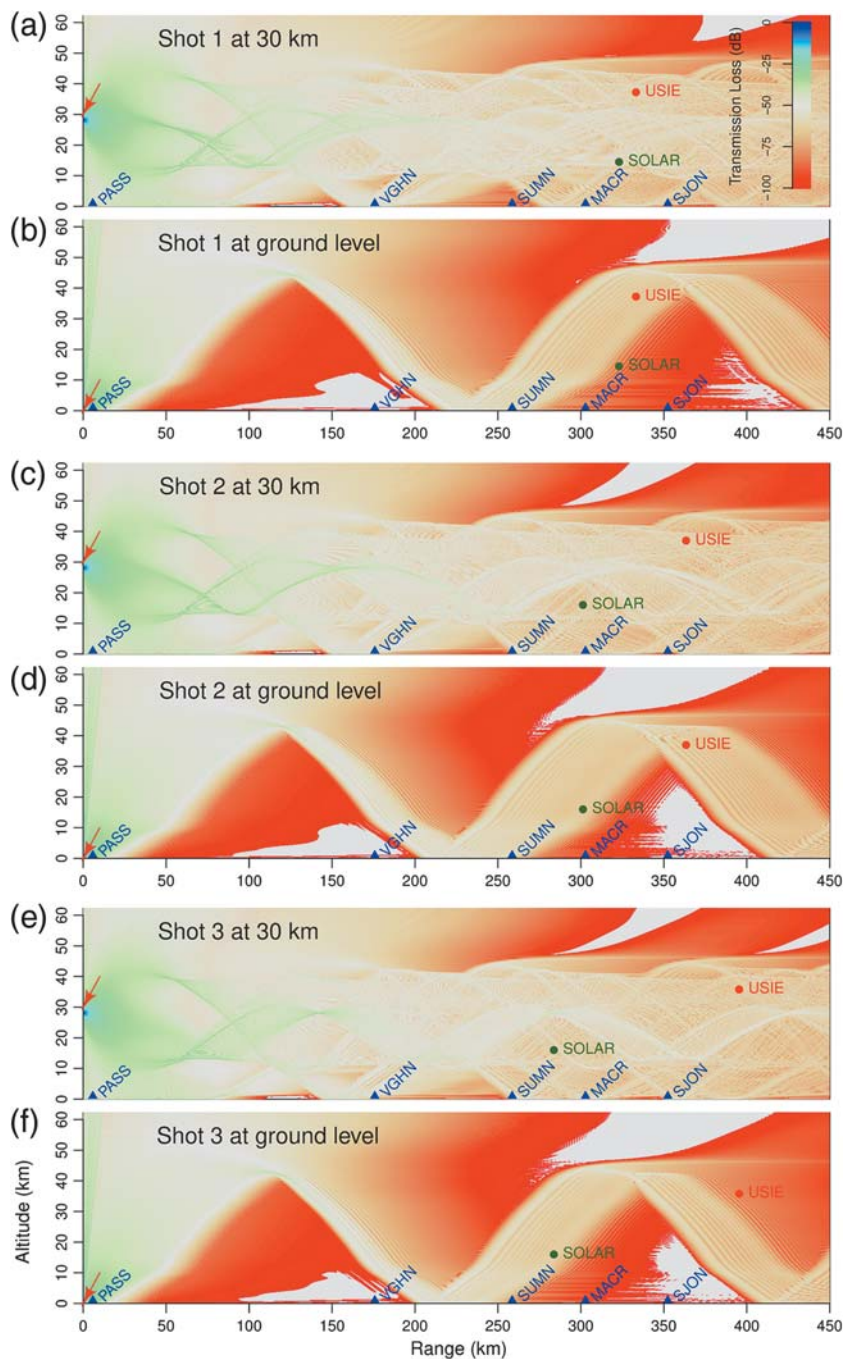
▲ **Figure 5.** Infrasound propagation patterns for (b,d,f) the ground-based explosions compared with the same source at (a,c,e) 30-km altitude. Propagation was modeled with *ncpaprop* and assumes the Ground to Space atmospheric model at the time of each explosion. Attenuation levels below −100 dB are not plotted.

efficiently channeled in a 10- to 50-km duct for the atmospheric conditions during the experiment. Acoustic attenuation is considerably less in this altitude range compared with the ground case; values between −25 and −50 dB extend to nearly 200 km. Furthermore, shadow zones do not exist in the acoustic channel. Shadow zones are present below 10 km, although they are much smaller in extent.

In summary, the models of bolides exploding at 30-km altitude suggest that balloon-borne sensors would detect sufficiently large explosions in the stratosphere in nearly all cases. Furthermore, the signals may propagate through the stratospheric duct without the usual r^{-1} attenuation of a spherically expanding wave. Finally, because of the many paths caused by ray turning points at the top and bottom of the duct, any signal from a bolide would be a combination of numerous arrivals coming from both above and below the balloon.

CONCLUSIONS

We arranged for three large ground explosions to take place near Socorro, New Mexico, and listened for the resulting infrasound disturbances from five ground stations and two balloon-borne sensor packages. Agreement between the model predictions and observations is generally good: signal strengths decrease as expected with altitude, delays between each explosion and the signal arrivals are consistent with plausible celerities for waves traveling in the stratospheric duct, and the distribution of ground stations in shadow zones matched the predicted locations of those zones, with the following proviso—the infrasound touch-down point was predicted to be 210–260 km from the explosion in shot 1 and 200–250 km in shots 2 and 3 but was actually shifted at least 60 km closer to the epicenter. As a result, the VGHN ground station observed shots 2 and 3, with only one possible observation on SUMN.

A key finding was the very low wind noise on balloon-borne platforms. Both the NASA balloon (at 37-km altitude) and the solar balloon (at 16 km) showed no detectable wind noise despite the lack of any physical wind filtering apparatus on the microphone ports on either payload.

Modeling results suggest that balloon-borne infrasound platforms would detect disturbances in the stratospheric duct. Long-duration super-pressure balloons would be well suited for campaigns to listen for bolides that explode in the Earth's atmosphere.

DATA AND RESOURCES

Infrasound and station metadata are publicly available and can be obtained from the Dryad Digital Repository under doi: http://dx.doi.org/10.5061/dryad.354kg7d. Acoustic velocity profiles are from the Ground to Space model (Drob *et al.*, 2003); these data will be archived in the Dryad repository as
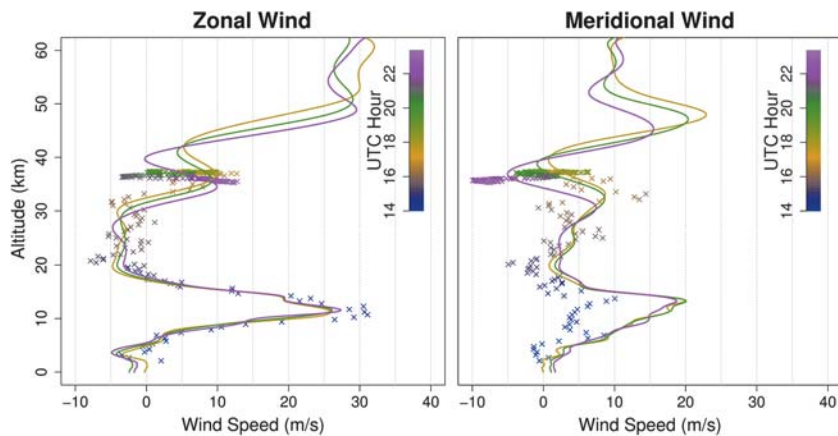
▲ **Figure 6.** Comparison of the horizontal motion of the zero pressure balloon with the Ground to Space model profiles used for the propagation predictions shown in Figure 5.
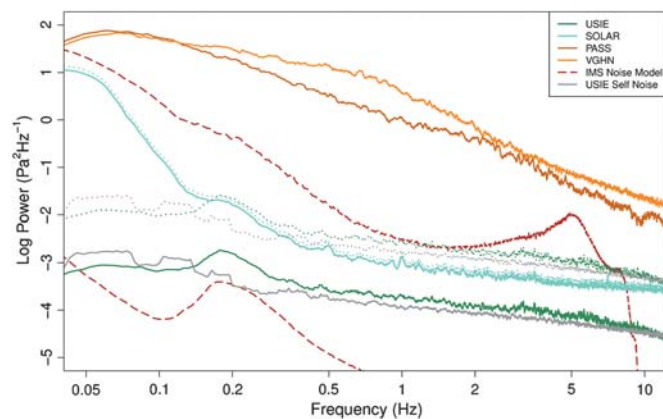
▲ **Figure 7.** Welch spectra of ground and free-flying stations from 20:00 to 23:00 UTC compared with the International Monitoring System (IMS) low- and high-noise models (Brown *et al.,* 2014). A 25-s Butterworth high-pass filter was applied to remove balloon oscillation signals from the spectra. Dotted lines represent balloon-borne stations adjusted for acoustic impedance contrasts relative to the National Oceanic and Atmospheric Administration (NOAA) Standard Atmosphere at sea level (NOAA, 1976). USIE, UNC-Sandia Infrasound Experiment.

well. The *ncpaprop* acoustic propagation model is publicly available from GitHub (https://github.com/chetzer-ncpa/ncpaprop, last accessed January 2017). The maps in Figure 1 were generated using the *ggmap* package in R (Kahle and Wickham, 2013). ⧖

ACKNOWLEDGMENTS

REFERENCES

Anderson, J. F., J. B. Johnson, D. C. Bowman, and T. J. Ronan (2018). The Gem infrasound logger and custom-built instrumentation, *Seismol. Res. Lett.* **89,** no. 1, 153–164.

Anderson, W. J., and I. Taback (1991). Oscillation of high altitude balloons, *J. Aircraft* **28,** no. 9, 606–608.

Arrowsmith, S. J., R. Burlacu, K. Pankow, B. Stump, R. Stead, R. W. Witaker, and C. Hayward (2012). A seismoacoustic study of the 2011 January 3 Circleville earthquake, *Geophys. J. Int.* **189,** 1148–1158.

Banister, J. R., and W. V. Hereford (1991). Observed high-altitude pressure waves from an underground and a surface explosion, *J. Geophys. Res.* **96,** no. D3, 5185–5193.

Blanc, E., L. Ceranna, A. Hauchecorne, A. Charlton-Perez, E. Marchetti, L. G. Evers, T. Kvaerna, J. Lastovicka, L. Eliasson, N. B. Crosby, *et al.* (2017). Toward an improved representation of middle atmospheric dynamics thanks to the ARISE project, *Surv. Geophys.* doi: 10.1007/s10712-017-9444-0.

Blom, P., O. Marcillo, and S. J. Arrowsmith (2016). Analysis and modeling of infrasound from a four-stage rocket launch, *J. Acoust. Soc. Am.* **139,** no. 6, 3134–3138.

Bowman, D. C., and S. A. Albert (2018). Acoustic event location and background noise characterization on a free flying infrasound sensor network in the stratosphere, *Geophys. J. Int.* doi: 10.1093/gji/ggy069.

Bowman, D. C., and J. M. Lees (2017). A comparison of the ocean microbarom recorded on the ground and in the stratosphere, *J. Geophys. Res.—Atmospheres* doi: 10.1002/2017JD026474.

Bowman, D. C., J. Taddeucci, K. Kim, J. F. Anderson, J. M. Lees, A. Graettinger, I. Sonder, and G. A. Valentine (2014). The acoustic signatures of ground acceleration, gas expansion, and spall fallback in experimental volcanic explosions, *Geophys. Res. Lett.* **41,** 1916–1922.

Brown, D., L. Ceranna, M. Prior, P. Mialle, and R. Le Bras (2014). The IDC seismic, hydroacoustic and infrasound global low and high noise models, *Pure Appl. Geophys.* **171,** 361–375.

Chunchuzov, I., S. Kulichkov, V. Perepelkin, O. Popov, P. Firstov, J. D. Assink, and E. Marchetti (2015). Study of the wind velocity-layered structure in the stratosphere, mesosphere, and lower thermosphere by using infrasound probing of the atmosphere, *J. Geophys. Res.—Atmospheres* **120,** 8828–8840.

Drob, D. P., J. M. Picone, and M. A. Garcés (2003). Global morphology of infrasound propagation, *J. Geophys. Res.* **108,** no. D21, 1–12.

Evans, L. B., H. E. Bass, and L. C. Sutherland (1972). Atmospheric absorption of sound: Theoretical predictions, *J. Acoust. Soc. Am.* **51,** 1565–1575.

Gi, N., and P. Brown (2017). Refinement of bolide characteristics from infrasound measurements, *Planet. Space Sci.* doi: 10.1016/j.pss.2017.04.021.

Green, D. N., and D. Bowers (2010). Estimating the detection capability of the International Monitoring System infrasound network, *J. Geophys. Res.* **115,** no. D18116, doi: 10.1029/2010JD014017.

Green, D. N., J. Vergoz, R. Gibson, A. Le Pichon, and L. Ceranna (2011). Infrasound radiated by the Gerdec and Chelopechene explosions: Propagation along unexpected paths, *Geophys. J. Int.* **185,** 890–910.

Ishihara, Y., Y. Hiramatsu, M. Yamamoto, M. Furumoto, and K. Fujita (2012). Infrasound/seismic observation of the Hayabusa reentry: Observations and preliminary results, *Earth Planets Space* **64,** 655–660.

Jolly, A. D., R. S. Matoza, D. Fee, B. M. Kennedy, A. M. Iezzi, R. H. Fitzgerald, A. C. Austin, and R. Johnson (2017). Capturing the acoustic radiation pattern of strombolian eruptions using infrasound sensors aboard a tethered aerostat, Yasur volcano, Vanuatu, *Geophys. Res. Lett.* **44,** doi: 10.1002/2017GL074971.

Kahle, D., and H. Wickham (2013). ggmap: Spatial visualization with ggplot2, *The R Journal* **5,** 144–161.

Krishnamoorthy, S., A. Komjathy, M. T. Pauken, J. A. Cutts, R. F. Garcia, D. Mimoun, A. Cadu, A. Sournac, J. M. Jackson, V. H. Lai, *et al.* (2018). Detection of artificially generated seismic signals using balloon-borne infrasound sensors, *Geophys. Res. Lett.* doi: 10.1002/2018GL077481.

Lally, V. E. (1967). Superpressure balloons for horizontal soundings of the atmosphere, *Technical Report*, National Center for Atmospheric Research.

Le Pichon, A., P. Herry, P. Mialle, J. Vergoz, N. Brachet, M. Garcés, D. Drob, and L. Ceranna (2005). Infrasound associated with the 2004–2005 large Sumatra earthquake and tsunami, *Geophys. Res. Lett.* **32,** L19802, doi: 10.1029/2005GL023893.

Le Pichon, A., J. Vergoz, E. Blanc, J. Guilbert, L. Ceranna, L. Evers, and N. Brachet (2009). Assessing the performance of the International Monitoring System's infrasound network: Geographical coverage and temporal variabilities, *J. Geophys. Res.—Atmospheres* **114,** no. D08112, doi: 10.1029/2008JD010907.

Lighthill, J. (1978). *Waves in Fluids*, Cambridge University Press, Cambridge, United Kingdom.

Lonzaga, J. B., R. M. Waxler, J. D. Assink, and C. L. Talmadge (2015). Modelling waveforms of infrasound arrivals from impulsive sources using weakly non-linear ray theory, *Geophys. J. Int.* **200,** 1347–1361.

Marcillo, O., J. B. Johnson, and D. Hart (2012). Implementation, characterization, and evaluation of an inexpensive low-power low-noise infrasound sensor based on a micromachined differential pressure transducer and a mechanical filter, *J. Atmospheric Ocean. Technol.* **29,** 1275–1284.

Matoza, R. S., D. N. Green, A. Le Pichon, P. M. Shearer, D. Fee, P. Mialle, and L. Ceranna (2017). Automated detection and cataloging of global explosive volcanism using the International Monitoring System infrasound network, *J. Geophys. Res.* **122,** 2946–2971.

Mentink, J. H., and L. G. Evers (2011). Frequency response and design parameters for differential microbarometers, *J. Acoust. Soc. Am.* **130,** no. 1, 33–41.

National Oceanic and Atmospheric Administration (NOAA) (1976). U.S. standard atmosphere, 1976, *Technical Report*, National Oceanic and Atmospheric Administration, National Aeronautics and Space Administration, and the United States Air Force.

Negraru, P. T., P. Golden, and E. T. Herrin (2010). Infrasound propagation in the "Zone of Silence," *Seismol. Res. Lett.* **81,** no. 4, 615–625.

Rayleigh, B. (1894). *The Theory of Sound*, Vol. 2, Macmillan and Co, New York, New York.

ReVelle, D. O. (1976). On meteor-generated infrasound, *J. Geophys. Res.* **81,** no. 7, doi: 10.1029/JA081i007p01217.

Silber, E. A., and P. G. Brown (2014). Optical observations of meteors generating infrasound—I: Acoustic signal identification and phenomenology, *J. Atmospheric Sol.-Terr. Phys.* **119,** 116–128.

Slad, G. W., and B. J. Merchant (2016). Chaparral Model 60 infrasound sensor evaluation, *Technical Report*, Sandia National Laboratories, SAND2016–1902.

Stroud, W. G., W. Nordberg, W. R. Bandeen, F. L. Bartman, and P. Titus (1960). Rocket-grenade measurements of temperatures and winds in the mesosphere over Churchill, Canada, *J. Geophys. Res.* **65,** no. 8, 2307–2323.

Sutherland, L. C., and H. E. Bass (2004). Atmospheric absorption in the atmosphere up to 160 km, *J. Acoust. Soc. Am.* **115,** no. 3, 1012–1032.

Waxler, R., L. G. Evers, J. Assink, and P. Blom (2015). The stratospheric arrival pair in infrasound propagation, *J. Acoust. Soc. Am.* **137,** no. 4, 1846–1856.

Waxler, R., K. E. Gilbert, and C. Talmadge (2008). A theoretical treatment of the long range propagation of impulsive signals under strongly ducted nocturnal conditions, *J. Acoust. Soc. Am.* **124,** 2742–2754.

Waxler, R., C. Hetzer, and D. Velea (2015). *Atmospheric Infrasound Propagation Package Version 1.1 Extension and Finalization*, The University of Mississippi, Oxford, Mississippi.

Weaver, R. L., and J. McAndrew (1995). *The Roswell Report: Fact Versus Fiction in the New Mexico Desert*, U.S. Government Printing Office, Washington, D. C.

Wescott, J. W. (1964). Acoustic detection of high-altitude turbulence, *Technical Report*, The University of Michigan.

Whitaker, R. W., and J. P. Mutschlecner (2008). A comparison of infrasound signals refracted from stratospheric and thermospheric altitudes, *J. Geophys. Res.—Atmospheres* **113,** no. D08117, doi: 10.1029/2007JD008852.

E. F. Young
C. Ballard[1]
Southwest Research Institute
1050 Walnut Street Suite 300
Boulder, Colorado 80302 U.S.A.

D. C. Bowman
S. J. Arrowsmith
Sandia National Laboratories
1515 Eubank SE, MS 0404
Albuquerque, New Mexico 87123 U.S.A.
dbowma@sandia.gov

J. M. Lees
Department of Geological Sciences
The University of North Carolina at Chapel Hill
104 South Road, Mitchell Hall, Campus Box #3315
Chapel Hill, North Carolina 27599 U.S.A.

V. Klein
Colorado Center for Astrodynamics Research
University of Colorado Boulder
ECNT 320, 431 UCB
Boulder, Colorado 80309 U.S.A.

[1] Now at Syncroness, Inc., 10875 Dover Street, Westminster, Colorado 80021 U.S.A.